High-Density Near-Ultraviolet Silicon Photomultipliers: Characterization of photosensors for Cherenkov light detection

Available online at www.sciencedirect.com

ScienceDirect

ELSEVIER

Nuclear Instruments and Methods in Physics Research A 00 (2023) 1–17

NIMA

High-Density Near-Ultraviolet Silicon Photomultipliers: characterization of photosensors for Cherenkov light detection

G. Ambrosi[a], M. Ambrosio[b], C. Aramo[b,*], B. Bertucci[a,c], E. Bissaldi[d,e,*], M. Bitossi[f], A. Boiano[b], C. Bonavolontà[b], M. Capasso[g], A. Circiello[b], L. Consiglio[b], D. Depaoli[h,i], F. Di Pierro[i], L. Di Venere[d,e,*], E. Fiandrini[a,c], N. Giglietto[d,e], F. Giordano[d,e], S. Incardona[j,k], M. Ionica[a], F. Licciulli[e], S. Loporchio[d,e], G. Marsella[j,k], V. Masone[b], F. R. Pantaleo[d,e], R. Paoletti[l,f], B. Ruggiero[m,b], A. Rugliancich[f], P. Silvestrini[n,b], L. Stiaccini[l,f], J. Tasseva[b], L. Tosti[a,c], G. Tripodo[j,k], V. Vagelli[a,o], M. Valentino[m,b]

[a] *INFN Sezione di Perugia, 06123 Perugia, Italy*
[b] *INFN Sezione di Napoli, 80126 Napoli, Italy*
[c] *Dipartimento di Fisica e Geologia dell'Università degli Studi di Perugia, 06123 Perugia, Italy*
[d] *Dipartimento Interateneo di Fisica dell'Università e del Politecnico di Bari, 70126 Bari, Italy*
[e] *INFN Sezione di Bari, 70125 Bari, Italy*
[f] *INFN Sezione di Pisa, 56127 Pisa, Italy*
[g] *Department of Physics and Astronomy, Barnard College, Columbia University, NY 10027, USA*
[h] *Dipartimento di Fisica dell'Università degli Studi di Torino, 10125 Torino, Italy*
[i] *INFN Sezione di Torino, 10125 Torino, Italy*
[j] *Dipartimento di Fisica e Chimica "E. Segrè", Università degli Studi di Palermo, via delle Scienze, 90128 Palermo, Italy*
[k] *INFN Sezione di Catania, 95123 Catania, Italy*
[l] *Dipartimento di Scienze Fisiche, della Terra e dell'Ambiente, Università degli Studi di Siena, 53100 Siena, Italy*
[m] *CNR-ISASI, 80078 Pozzuoli, Italy*
[n] *Università Della Campania "Luigi Vanvitelli", 81100 Caserta, Italy*
[o] *Agenzia Spaziale Italiana, 00133 Roma, Italy*

Abstract

In recent years, Silicon Photomultipliers (SiPMs) have proven to be highly suitable devices for applications where high sensitivity to low-intensity light and fast responses are required. Among their many advantages are their low operational voltage when compared with classical photomultiplier tubes, mechanical robustness, and increased photon detection efficiency (PDE).

Here we present a full characterization of a SiPM device technology developed in Italy by Fondazione Bruno Kessler, which is suitable for Cherenkov light detection in the Near-Ultraviolet (NUV) band. This device is a High-Density (HD) NUV SiPM, based on a microcell of 40 μm × 40 μm and with an area of 6 × 6 mm^2, providing low levels of dark noise and high PDE peaking in the NUV band. This particular device has been selected to equip a part of the focal plane of the Schwarzschild-Couder Telescope (SCT) prototype proposed for the Cherenkov Telescope Array (CTA) Observatory.

Keywords:
silicon photomultipliers, Cherenkov telescopes, very-high-energy astrophysics

1. Introduction

In recent years, Silicon Photomultipliers (SiPMs) are being widely tested and used for applications in which response to fast and low-intensity light signals is required. The small pixel size and the relatively low cost per channel make these devices interesting also for applications in which a deep imaging resolution is necessary.

This is particularly true for cameras employed in the very-high-energy gamma-ray astrophysics field. Major Imaging Atmospheric (or Air) Cherenkov Telescopes (IACTs) cameras operating since the mid-'80s have been employing photomultiplier tubes (PMTs). However, over the past 10 years, the great advancement in solid-state photosensors has proven those SiPMs whose efficiency is maximized for the detection of near-ultraviolet (NUV) wavelengths to represent a valid alternative to the PMT technology. Their single-photon-counting capability represents a powerful tool for signal calibration, and their compactness and low operational voltage (<100 V) allow a significant simplification of the camera design.

*Corresponding authors
Email addresses: aramo@na.infn.it (C. Aramo), elisabetta.bissaldi@ba.infn.it (E. Bissaldi), leonardo.divenere@ba.infn.it (L. Di Venere)

The first such sensors to be mounted on an IACT were Geiger-mode Avalanche Photodiodes (G-APDs), which offered a high gain and demonstrated the crucial capability to be operated under much brighter light conditions, allowing observations during moon time. A fully equipped camera based on G-APDs was successfully mounted on the First G-APD Cherenkov Telescope (FACT), installed in 2011 at the Observatorio del Roque de los Muchachos in La Palma (Canary Islands, Spain) [1]. Over the past years, the excellent and stable performance of FACT's camera allowed for consistent measurements and increased the observation time around the full moon, for a total of ∼14000 hours of physics data recorded [2].

The Cherenkov Telescope Array (CTA) project is a multinational, worldwide project to build a new generation of ground-based gamma-ray instruments[1]. Currently, the CTA Consortium includes ∼1500 members from more than 150 institutes in 25 countries. The first concept behind CTA was born in 2005. Right from the start, it aimed to achieve a factor of 5-10 improvement in sensitivity in the 100 GeV to 10 TeV range with respect to operating facilities, and to extend to energies well below 100 GeV and above 100 TeV by means of tens of IACTs [3]. These will be arranged in two arrays, one in the Northern hemisphere, at the Observatorio Roque de Los Muchachos in La Palma on the Canary Islands, and the other one in the Southern Hemisphere next to the European Southern Observatory's (ESO's) existing Paranal Observatory in the Atacama Desert, in Chile. The plan is to operate CTA as an open observatory [4].

In October 2013, the Italian Ministry approved the funding of a Research and Development (R&D) study, within the *Progetto Premiale TElescopi CHErenkov made in Italy* (TECHE.it), devoted to the development of a demonstrator for a camera for CTA. A joint venture between several Universities, the Italian National Institute for Nuclear Physics (INFN), the Italian National Institute for Astrophysics (INAF), and various industrial partners designed and constructed a very compact camera demonstrator, made by nine photo-sensor modules equipped with NUV SiPMs produced by Fondazione Bruno Kessler (FBK)[2] in Italy, Front-End Electronics (FEE) based on the TARGET-7 ASIC, a 16-channel fast sampler (1 GS/s) with deep buffer, self-trigger, and on-demand digitization capabilities [5].

In 2015, the Italian venture joined the consortium of US institutions organized to construct a prototype Schwarzschild-Couder telescope (pSCT)[3] with a 9.7 m aperture to test the feasibility of an innovative SC Medium Sized Telescope (MST) design for the CTA observatory [6]. The pSCT construction started in fall 2015 at the Fred Lawrence Whipple Observatory in Arizona (USA). At that time, an agreement was reached to equip a section of the focal plane of the pSCT telescope with Italian SiPMs produced by FBK [7]. The design of the camera foresees 11328 $6 \times 6\,\mathrm{mm}^2$ SiPM pixels, arranged in 64-pixel detection modules. Currently, the only equipped sector of the camera hosts 1536 pixels, out of which 576 are FBK SiPMs while the rest are Hamamatsu S12642-0404PA-50(X) SiPMs. For further details on the pSCT camera, the reader is addressed to [8].

Assembly and testing of the camera were completed in early May 2018, and it was installed on the telescope at the end of the same month. The pSCT was inaugurated in January 2019 [9, 10]. A few days later, the telescope recorded its first light, including its first detection of particle showers. Even with the reduced number of installed pixels, the telescope successfully proved the feasibility of the design. Recently, the SCT collaboration announced the detection of TeV gamma rays from the Crab Nebula, proving the viability of the novel telescope design in gamma-ray astrophysics [11].

1.1. Evolution of FBK SiPM devices and the synergy with INFN

FBK has been developing SiPMs since 2006 [12]. Different technologies and designs have been implemented since that time to improve the device performance. The optimization process involved simulations, design, fabrication, production, and characterization [13]. The synergy between FBK and INFN contributed to the development of an *ad-hoc* research line of highly sensitive photon detectors dedicated to Cherenkov applications. The basic structure of these SiPMs consists of a p^+-n junction whose design was optimized by FBK for the detection in the blue-NUV region of the electromagnetic spectrum [14, 15]. In particular, FBK progressively improved NUV SiPM technology focusing mainly on the optimization of the active high-field region with the aim of increasing the avalanche triggering probability, decreasing the dark count rate (DCR), and enhancing the uniformity and temperature stability [16]. Maintaining the same device structure, they finally optimized the silicon material to mitigate the delayed correlated noise [17]. In

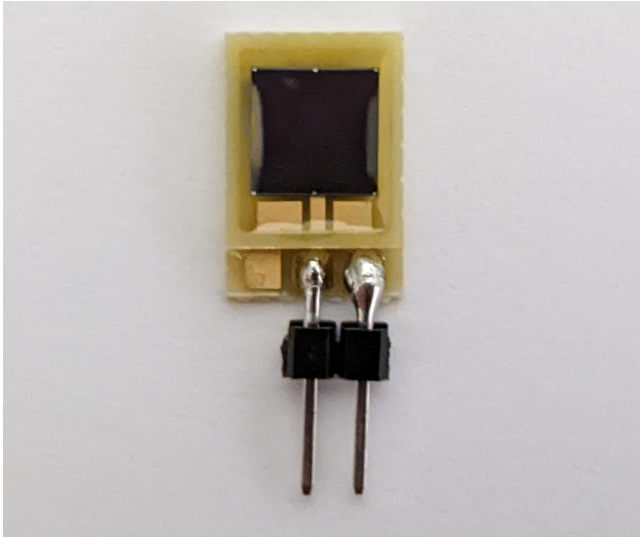

Figure 1: Picture of a FBK NUV-HD SiPM (HD3) with an area of $6 \times 6\,\mathrm{mm}^2$ and a $40\,\mu$m-cell pitch. The SiPM is covered by an UV-transparent epoxy resin which acts as a shielding.

[1] For more details please visit `https://www.cta-observatory.org/`

[2] `https://srs.fbk.eu/`

[3] `https://cta-psct.physics.ucla.edu/`

Table 1: Summary of FBK NUV-HD SiPMs tested for this work and their characteristics

Device type	Size $[\mathrm{mm}^2]$	Cell pitch $[\mu\mathrm{m}]$
HD1	6×6	30
HD3	6×6	40

order to further improve the characteristics of the NUV technology in terms of optical cross-talk (CT), photodetection efficiency (PDE), and dynamic range, FBK introduced in 2016 new SiPMs with a cell pitch down to 15 μm, optical trenches to better isolate the microcells and fill factor (FF) much higher compared to the previous generation of SiPMs, the so-called NUV-HD (high-density) SiPMs [18, 19].

Different types of NUV-HD devices were tested between 2016 and 2018 at the INFN laboratories in Italy, including those of the Bari, Napoli, Perugia, and Pisa units, in order to verify and compare their performances. The first results on the first generation of NUV-HD SiPMs (which we refer to as HD1) with an area of $6 \times 6\,\mathrm{mm}^2$ and pitch of 30 μm are reported in [20]. The evolution of the technology led to the production of SiPMs with an area of $6 \times 6\,\mathrm{mm}^2$ and an increased pitch of 40 μm, which have been employed for the pSCT camera [8]. We refer to these devices as HD3 (see Table 1). A picture of a FBK NUV-HD SiPM (HD3) is shown in Figure 1.

In order to characterize the SiPMs and to determine their main properties, we separately tested devices with an active area of $1 \times 1\,\mathrm{mm}^2$ and $6 \times 6\,\mathrm{mm}^2$. In this work we focus on the performance of the SiPM selected for the pSCT camera, the FBK NUV-HD3 $6 \times 6\,\mathrm{mm}^2$ SiPMs, specifically developed for CTA applications. We report the characterization measurements of the HD3 devices, comparing their performances with the first generation of $6 \times 6\,\mathrm{mm}^2$ NUV-HD (HD1) devices, focusing on the results available for both technologies.

The paper is organized as follows. In Section 2 we present the results of the static (DC) measurements performed at INFN Bari, leading to the estimation of the breakdown voltage at different temperatures, a parameter which is fundamental for subsequent measurements. Results of the dynamic characterization are given in Section 3. These parameters provide guidance on defining the operational conditions when using SiPMs and are extracted during the normal operation of the device. They include gain and its dependence on the bias voltage, correlated noise, recovery time and DCR. The photon detection efficiency determination is presented in Section 4 and shows measurements performed at INFN Napoli at different wavelengths (from 400 to 880 nm) and various incident angles of the radiation. Finally, in Section 5 we draw our conclusions.

2. Static characteristics

We first discuss the current-voltage (IV) characteristics of the tested devices. The IV characteristic measurement can be achieved by acquiring the current measured by the power supply, i.e. measuring the current drain of the sensor as a function of the bias voltage. We made use of a Keithley 2400 Source Meter Unit (SMU) in order to provide the bias voltage V_b and to measure the SiPM output current I in DC mode. We tested the temperature dependence of the IV characteristics by placing the devices in a light-proof climate chamber (ACS Compact Test Chamber Model DY16T) in total dark conditions. We placed a thermocouple right behind the SiPM in order to measure the temperature directly on the device. We connected a DAQ computer to both the SMU and the climate chamber, in order to set the desired chamber temperature and simultaneously check the thermocouple temperature during data acquisition. A scheme of the setup is shown in Figure 2. We sampled the forward and reverse IV curves in a temperature range between -15°C and 35°C in steps of 5°C.

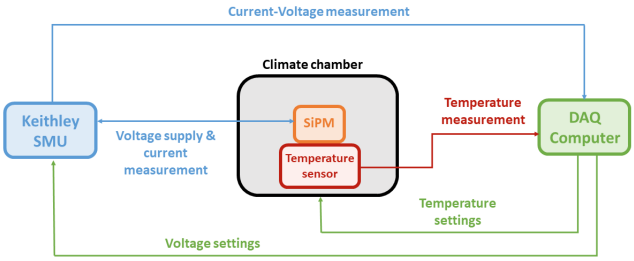

Figure 2: Scheme of the setup used to measure the IV characteristics of the SiPMs.

2.1. Breakdown voltage

The reverse IV curve allows the measurement of the breakdown voltage V_BD of the device, which is needed to correctly polarize it in the G-APD regime. All the properties described in the following sections are given as a function of the applied over-voltage (OV), i.e. the difference between the bias voltage and the breakdown voltage: $V_\mathrm{OV} = V_\mathrm{b} - V_\mathrm{BD}$. If $V_\mathrm{OV} > 0$, the avalanche photodiodes in a SiPM are in Geiger mode. The over-voltage represents a key adjustable parameter affecting the operation and performance of a SiPM.

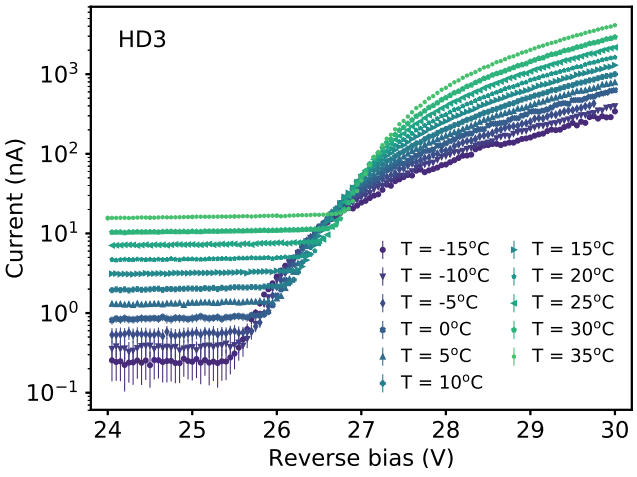

Figure 3: Reverse Current-Voltage (IV) curves measured at different temperatures for the NUV-HD3 SiPM.

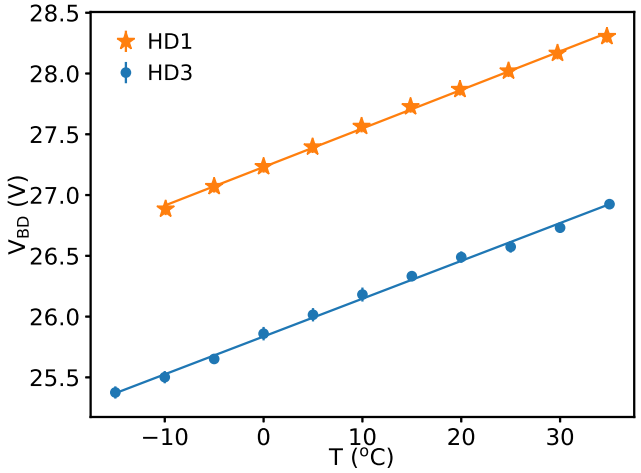

Figure 4: Temperature dependence of the breakdown voltage between T = −15°C and T = 35°C for HD1 (orange stars) and HD3 (blue dots) devices. A linear fit is superimposed to the data (solid curves).

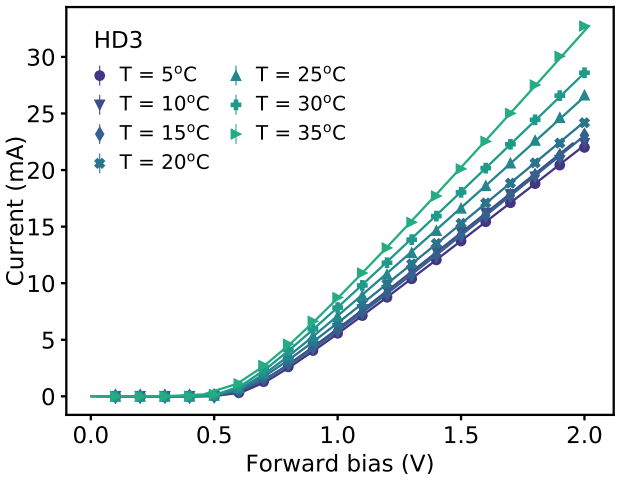

Figure 5: Forward Current-Voltage (IV) curves measured at six different temperatures between T = 5°C and T = 35°C in steps of 5° for the NUV-HD3 SiPM. The solid curves represent the best fit curves obtained with Equation (2).

Figure 3 shows the acquired reverse IV curves at different temperatures. In order to correctly derive the values of the breakdown voltage, we follow a method proposed by [21], which is based on [22, 23]. As already noted by [12] and further explained by [21], the IV curve of individual SiPM cells (also called single-photon avalanche photodiodes or SPADs) can be described by a parabola above the breakdown. To obtain the breakdown voltage from an IV curve, [23] proposes using the voltage where $(dI/dV_b)/I$ is maximal, whereas [22] proposes using the maximum of $dln(I(V_b))/dV_b$. [21] verified how both methods are equivalent and yield identical results:

$$\frac{dI/dV_b}{I} = \frac{dlnI(V_b)}{dV_b} = \frac{2}{V_b - V_{BD}}\,. \quad (1)$$

Results for the breakdown voltage determination at different temperatures for the tested HD1 and HD3 SiPMs are given in Figure 4. The slopes of the linear fits applied to the measurements reveal the same temperature dependence β for both devices (within the error), namely $\beta_{HD1} = (31.7 \pm 0.4)\,mV/°C$ and $\beta_{HD3} = (31.1 \pm 0.5)\,mV/°C$. At room temperature (T = 25°C), we find that $V_{BD,\,HD1} = (28.01 \pm 0.04)$ V and $V_{BD,\,HD3} = (26.49 \pm 0.02)$ V. Uncertainties are obtained from the fit procedure taking into account the errors on individual measurements. We note that these values are in perfect agreement with those reported by FBK in [19].

2.2. Quenching resistor and saturation current

A SiPM consists of N_{cell} p-n junctions connected in parallel [24]. The microcells behave as diodes with a series resistor known as quenching resistor. The resulting forward IV curves shown in Figure 5 can be approximated with a Shockley diode law with an additional resistive component given by the parallel of the N_{cell} quenching resistors R_q [24]. We fitted the Voltage-Current (VI) curves with the following equation:

$$V = n_{id} V_T \cdot \ln\left(\frac{I}{I_s} + 1\right) + R_s \cdot I\,, \quad (2)$$

where V is the applied voltage, n_{id} is the ideality factor, V_T is the thermal voltage, I is the measured current, I_s is the saturation current, and R_s results from the parallel connection of N_{cell} quenching resistors, i.e. $R_s = R_q/N_{cell}$. Having a cell pitch of 40 μm, we calculated the number of cells for the 6×6 mm^2 HD3 devices as $N_{cell} = (6\,mm/40\,\mu m)^2 \approx 22500$. We point out that we performed the analysis of the forward IV measurements only for positive temperatures above 5°C. At lower temperatures the effect of the device heating up due to the intense current (∼ mA) prevented to keep a stable temperature on the SiPM surface.

For each temperature, we estimated n_{id}, R_s and I_s from the fit reported in Figure 5. The value of n_{id} is weakly changing with temperature, ranging between 1.2 and 1.5, while the temperature dependence of R_q and I_s are shown in Figures 6 and 7, respectively. It can be seen that R_q decreases with temperature, from ∼1.30 MΩ at 5°C to ∼1 MΩ at 35°C. The dependence is

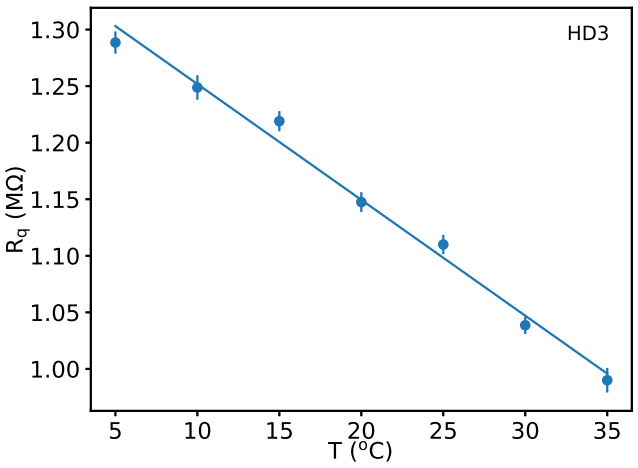

Figure 6: Quenching resistance R_q measured at different temperatures between T = 5°C and T = 35°C in steps of 5° for the NUV-HD3 SiPM. A linear fit is superimposed to the data (solid curve).

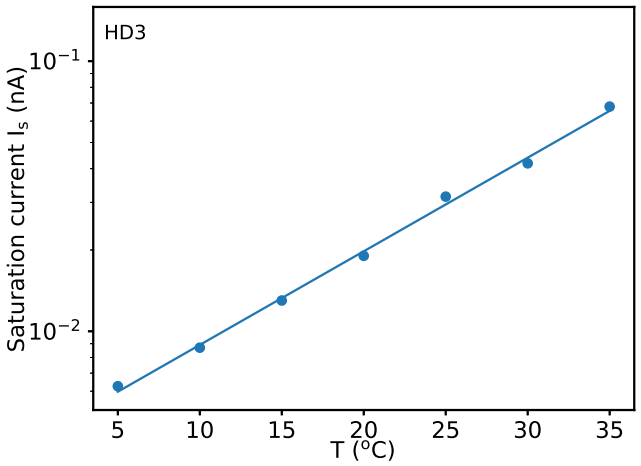

Figure 7: Saturation current I_s measured at different temperatures between T = 5°C and T = 35°C in steps of 5° for the NUV-HD3 SiPM. Note that I_s is displayed in logarithmic scale. A linear fit is superimposed to the data (solid curve).

almost linear with a coefficient of $(-10.2 \pm 0.4)\,\mathrm{k\Omega/°C}$. This behaviour is strictly related to the SiPM technology and depends on the internal structure of the poly-silicon quenching resistor [19]. The saturation current displayed in logarithmic scale in Figure 7 is exponentially increasing from ~6 pA at 5°C to ~70 pA at 35°C, due to the increase in the carriers' intrinsic concentration in the material.

3. Dynamic characteristics

In the following we present a dynamic characterization of the studied SiPMs, which extracts parameters that are crucial for the operation of a SiPM, such as the gain, the signal-to-noise ratio (SNR), the correlated noise, the recovery time, and the dark count rate.

Figure 8 shows the scheme of the experimental setup. We carried out all measurements in the same light-proof climate chamber used for the static characterization and repeated them at different temperatures. In order to illuminate the devices, we employed a picosecond laser emitting at 375 nm operated in pulse mode and controlled by a Pulse Diode Laser Driver (PicoQuant PDL 800-B). The laser driver was controlled by a pulse generator, whose signal was also sent to a 1 GHz Lecroy oscilloscope to trigger the acquisitions (Lecroy HDO 6104). The light intensity was set such that only a few photons per event could be detected by the SiPM. The SiPM signal was amplified with a commercial analog FEE board[4] consisting of an operational amplifier in transimpedance configuration followed by a gain stage.

Measurements were carried out in a temperature range between −10°C and 20° in steps of 10°C. For each temperature setting, we collected a few thousand waveforms over a wide bias voltage interval, approximately between 2 V and 13 V of OV.

[4] https://advansid.com/products/product-detail/asd-ep-eb-n

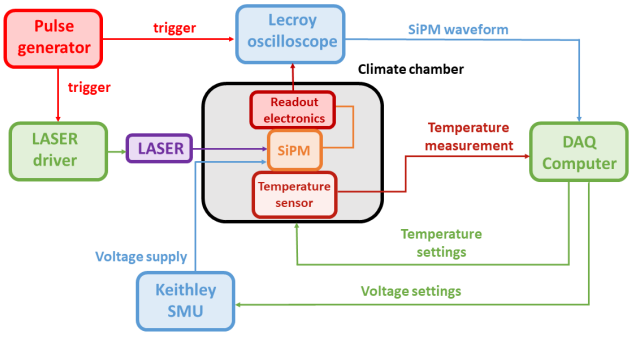

Figure 8: Scheme of the setup used to measure the dynamic characteristics of the SiPMs.

A collection of waveforms measured at V_{OV} = 4.9 V and T = 10°C for the HD3 device is shown in Figure 9. It can be clearly seen how SiPM signals typically present a sharp rising edge of hundreds of ps followed by a slower tail from tens to hundreds of ns, which depends on several parameters such as the junction capacitance, the quenching resistor and its parasitic capacitance, the size of the device and the input resistance of the FEE. The amplitude and the integral of the signal are both related to the number of photons simultaneously detected (see section 3.2 for more details). Thanks to the very low noise of the devices tested and of the selected FEE, single photo-electron (p.e.) signals can be easily distinguished, highlighting the photon counting capabilities of these devices.

In our anaysis, we first evaluated the baseline of each waveform by averaging the signal over a 200 ns-long time interval before the onset of the laser induced signal. We then subtracted this baseline value from the whole waveform. We note that this procedure is crucial in order to get rid of the DC offset due to the pre-amplifier. Subsequently, we analyzed the SiPM signals in terms of amplitude, by determining the peak amplitude of the waveform, and in terms of charge, by integrating the waveform from the onset of the signal up to a certain integration time and dividing by the transimpedance gain of the FEE. Both methods

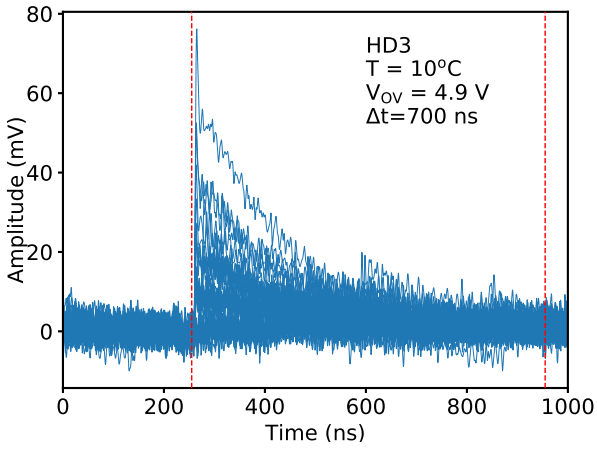

Figure 9: Collection of waveforms for the NUV-HD3 SiPM acquired at T = 10°C and V_{OV} = 4.9 V. Vertical dashed lines mark the beginning and the end of the 700-ns-long integration interval used for the charge analysis.

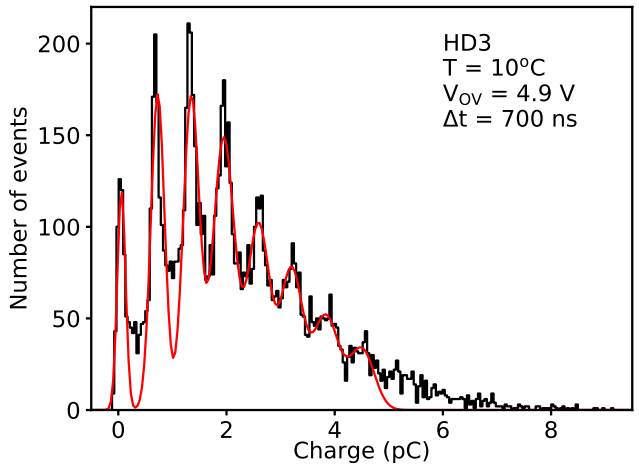

Figure 10: Charge distribution obtained from the analysis of the waveforms presented in Figure 9. The charge is calculated over an integration time of 700 ns, starting at the onset of the signal. A multi-gaussian fit (red solid curve) is superimposed on experimental data.

provide totally consistent results, thus in the following paragraph we present parameters obtained from the charge analysis unless otherwise stated.

Figure 10 shows the charge distribution resulting from the analysis of the waveforms presented in Figure 9. This distribution was obtained by integrating all waveforms over a time interval long enough to cover the whole tail of the signal (700 ns, indicated by the vertical dashed lines in Figure 9) and by dividing the result by the transimpedance gain of the FEE amplifier. All spectra are characterized by equally spaced peaks which represent the number of fired microcells. Although the response of smaller devices has a better resolution than that of larger ones [25], 6×6 mm^2 devices can also distinguish the number of photons that started an avalanche in the silicon active areas down to the single photo-electron.

Each peak can be modelled as a Gaussian function with a sigma driven by the fluctuations of the voltage at which the avalanche stops, structural differences between cells in the single SiPM, and noise introduced by the readout electronics. In order to quantify the performances of the devices, we fitted the histograms of amplitudes and charges using a parametrization based on the sum of Gaussian distributions. The fitting function used is given by:

$$\mathcal{M}(x) = \sum_{i=0}^{N} a_i \, \mathcal{G}(x; \mu_i, \sigma_i) \,, \qquad (3)$$

where x represents the central value of each histogram bin, $\mathcal{G}(x; \mu_i, \sigma_i)$ is a normalized Gaussian distribution with mean μ_i and width σ_i, and a_i is the normalization factor of the i-th component. The sum runs up to an arbitrary number N that depends on the number of populations resolved in the distribution, or equivalently to the maximum number of fired SiPM microcells that are statistically significant. The number of events with i fired microcells is then evaluated by the integral of the i-th component $a_i \, G(x; \mu_i, \sigma_i)$.

3.1. Gain and Signal-to-Noise Ratio

We evaluated the SiPM gain by analysing the 6×6 mm^2 devices. We integrated the full tail of the waveforms up to 700 ns after the signal onset, in order to estimate the full charge of each event. The absolute gain is obtained dividing the charge associated to a single p.e. by the electron charge.

The top panel of Figure 11 shows the gain as a function of the applied over-voltage of the HD3 SiPM at four different temperatures (from −10°C to 20°C). Measurements at T = 20°C (light green crosses) are limited to a smaller OV range, given the excessively high SiPM noise at OV values greater than 8 V. All data points are compatible within statistical uncertainties, hence no temperature dependence of the gain is observed. The gain dependence on the OV is evaluated with a linear fit and ranges between $(7.1 \pm 0.1) \cdot 10^5$/V and $(7.4 \pm 0.6) \cdot 10^5$/V, corresponding to a total cell capacitance of (113.7 ± 1.6) fF and (118.5 ± 9.6) fF, respectively.

In order to highlight the improvement of the FBK NUV-

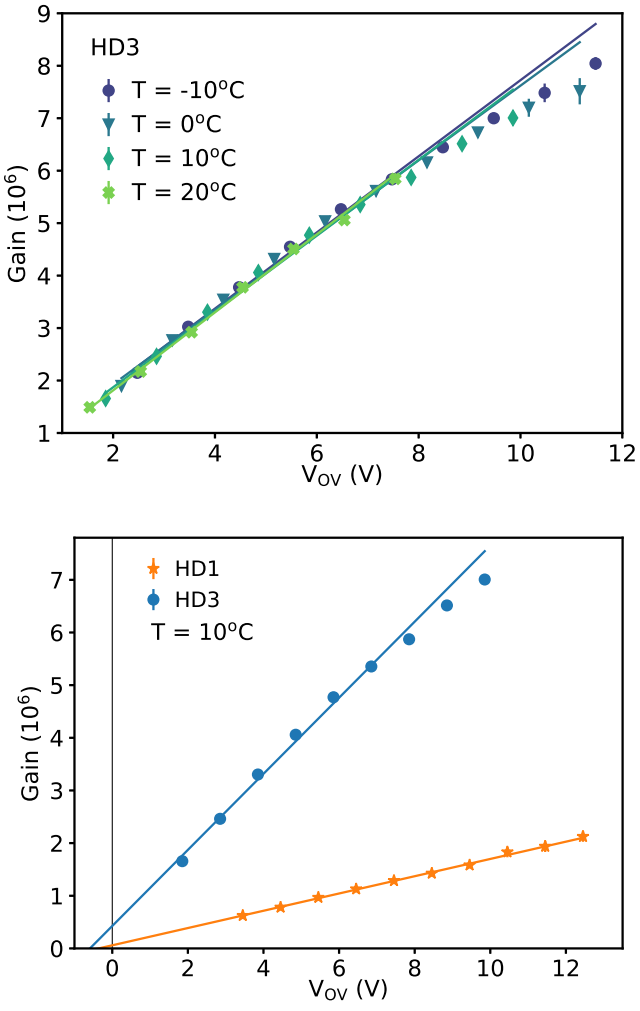

Figure 11: Gain as a function of the applied over-voltage for the HD3 SiPM at different temperatures (top panel) and for HD1 and HD3 SiPMs at a fixed temperature T = 10°C (bottom panel). Linear fits (solid lines) are shown superimposed on experimental data.

HD3 SiPMs over the first generation of NUV devices (HD1), we compare their absolute gain at an exemplifying temperature of T = 10°C, as can be seen in the bottom panel of Figure 11. At the same OV, HD3 SiPMs exhibit an overall gain that is much larger than the HD1 SiPMs' one, reaching a value of $(4.01\pm0.02)\cdot10^6$ for 5 V of OV. This difference can be explained by the fact that the two devices have a different microcell area. Moreover, the gain dependence from the OV is smaller for HD1 SiPMs ($(1.6 \pm 0.1) \cdot 10^5$/V) with respect to HD3 SiPMs ($(7.0 \pm 0.1) \cdot 10^5$/V).

We note that the extrapolation of the linear fit to zero gain provides an alternative method to infer the breakdown voltage of the device [21]. The bottom panel of Figure 11 shows that this value (V_{BD}^{Gain}) is smaller than the one derived in Section 2.1 (V_{BD}), the difference $\Delta V_{BD} = V_{BD} - V_{BD}^{Gain}$ being $\Delta V_{BD} = (0.59\pm0.02)$ V for HD3 SiPMs (~2.2%) and $\Delta V_{BD} = (0.36 \pm 0.09)$ V for HD1 SiPMs (~1.3%) at T = 10°C. This minor effect, extensively discussed in [21] and [26], where results of various methods used to determine the breakdown voltages of various types of SiPMs are compared, might be due to systematic uncertainties in the calibration of the signal chain used in the dynamic characteristic setup.

Next we evaluated the single p.e. SNR for each device, defined as the ratio of the gain per p.e. divided by the standard deviation of the pedestal. Figure 12 shows the evolution of the SNR as a function of the applied over-voltage. In the top panel we investigate the SNR of the HD3 SiPM at four different temperatures (from −10°C to 20°C). At lower temperatures the SNR significantly improves thanks to the reduced electronic noise of the system. As can be seen in the bottom panel of Figure 12, at a temperature T = 10°C HD3 SiPMs can reach a SNR as high as ~ 9 for $V_{OV} > 5$ V, while HD1 SiPMs only reach a maximum value of SNR ~ 8 at $V_{OV} > 10$ V. We point out that the quoted values are not an absolute indication of the SNR which finally depends on the different measurement conditions and distinct readout electronics (see [8] for more details regarding the NUV-HD3 SiPM application in the pSCT camera).

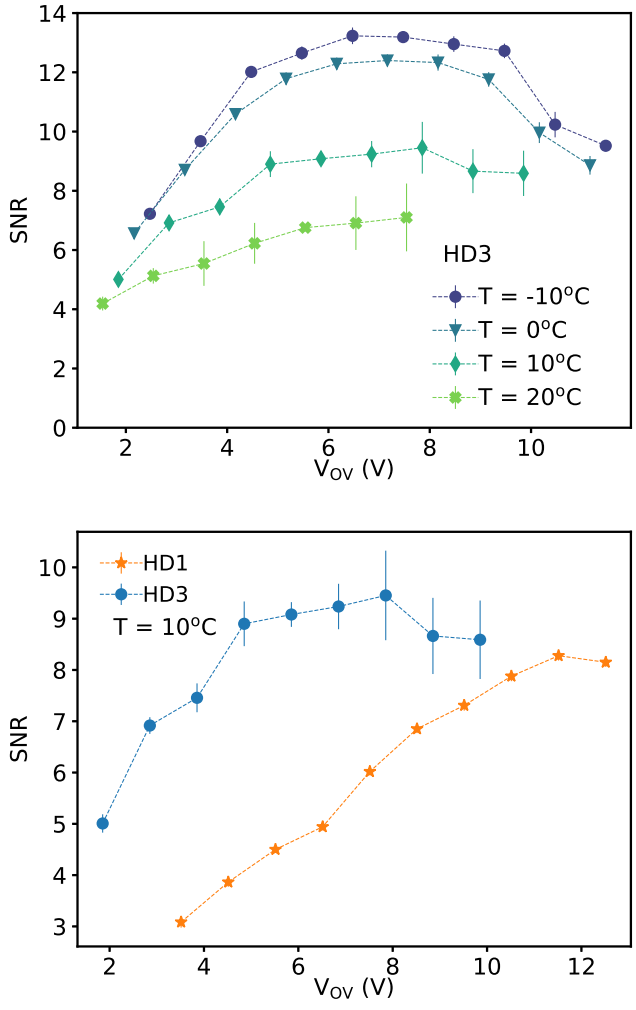

Figure 12: SNR as a function of the applied over-voltage for the HD3 SiPM at different temperatures (top panel) and for HD1 and HD3 SiPMs at a fixed temperature T = 10°C (bottom panel). The dashed lines only connect experimental data and do not represent an analytical fit.

3.2. Correlated noise

In order to evalute the SiPM's correlated noise, we analyzed the multi-gaussian charge distributions obtained by integrating the waveforms presented in Figure 9 over a shorter time interval of 30 ns, as shown in Figure 13. The choice of a shorter integration time is necessary in order to avoid the delayed correlated noise and dark pulses entering in the integration window.

Refering to equation 3, we extracted the area parameters a_i of the individual peaks, which represent the number of occurrence of zero, one, two, ..., i photo-electrons, whose distribution follows the photon statistics. Following the prescription suggested in [27], we parametrised it with a compound Poisson distribution, which takes into account the Poissonian behaviour of the number of photons detected in the SiPM microcells and

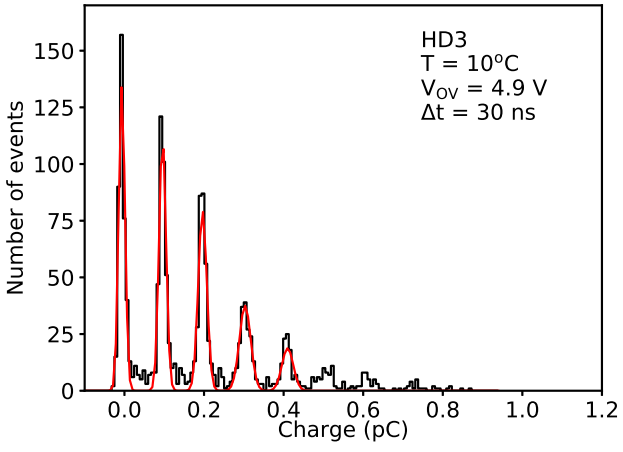

Figure 13: Charge distribution obtained from the analysis of the waveforms presented in Figure 9. The charge is calculated over an integration time of 30 ns, starting at the onset of the signal. A multi-gaussian fit (red solid curve) is superimposed on experimental data.

the cross-talk between microcells:

$$f_k(n_{pe}, p) = \frac{e^{-n_{pe}} \sum_{i=0}^{k} B_{i,k} \left[n_{pe}(1-p)\right]^i \cdot p^{k-i}}{k!}$$
$$B_{i,k} = \begin{cases} 1 & \text{if } i = 0 \text{ and } k = 0 \\ 0 & \text{if } i = 0 \text{ and } k > 0 \\ \frac{k!(k-1)!}{i!(i-1)!(k-i)!} & \text{otherwise} \end{cases} \quad (4)$$

The distribution $f_k(n_{pe}, p)$ for the number of events with k fired microcells depends on the average number of converting photons n_{pe} and on the cross-talk probability or correlated noise probability, p, and it reduces to a standard Poisson distribution with mean n_{pe} for the case $p = 0$. We refer to [27] for the details of the analytical parametrization.

The value of n_{pe} normalized to its maximum value gives an estimate of the relative photon detection efficiency (PDE). Figures 14 and 15 show the best fit values obtained for n_{pe} (normalized to its maximum) and for the cross-talk probability p, respectively, for the HD3 device at four different temperatures (top panels) and for the HD1 and the HD3 device at a fixed temperature T = 10°C (bottom panels).

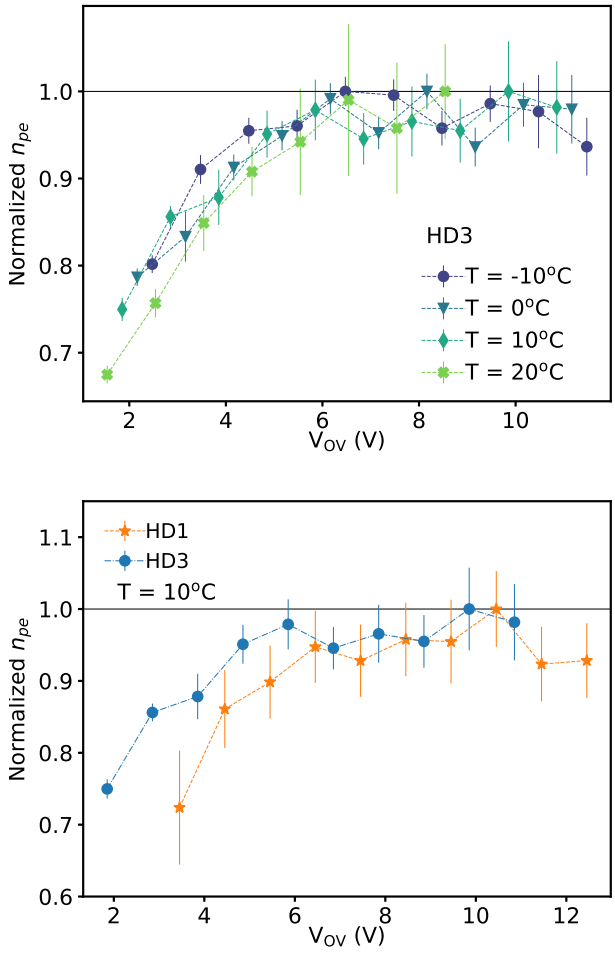

Figure 14: Normalized photoelectron yield (n_{pe}, normalized to its maximum value) as a function of the applied over-voltage for the HD3 SiPM at different temperatures (top panel) and for HD1 and HD3 SiPMs at a fixed temperature T = 10°C (bottom panel). The dashed lines only connect experimental data and do not represent an analytical fit.

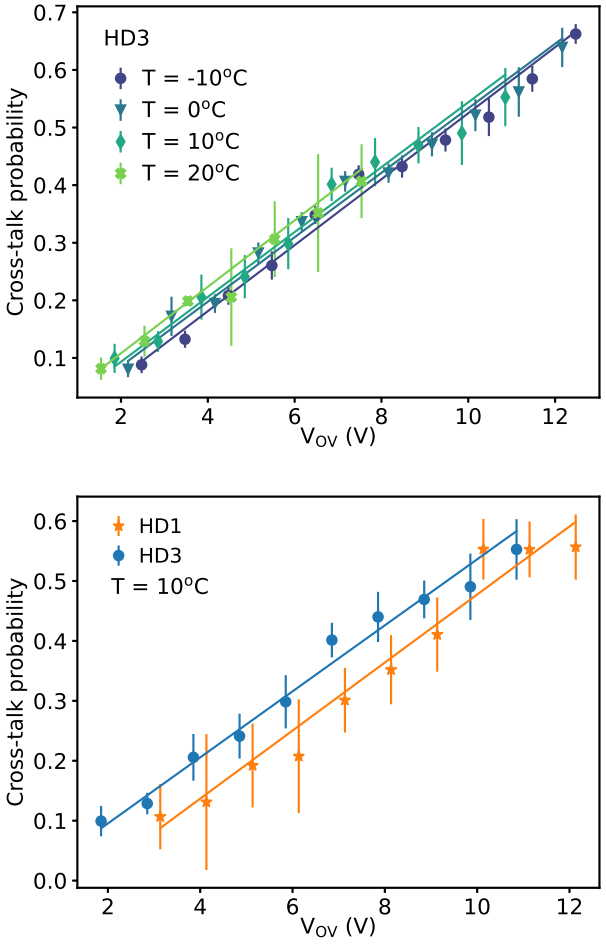

Figure 15: Cross-talk probability as a function of the applied over-voltage for the HD3 SiPM at different temperatures (top panel) and for HD1 and HD3 SiPMs at a fixed temperature T = 10°C (bottom panel). Linear fits (solid lines) are shown superimposed on experimental data.

As can be seen in both panels of Figure 14, the relative PDE always increases up to a certain OV value and then saturates to a constant level above this voltage. This information is crucial when choosing the best operating voltage of the devices. The values measured at different temperatures (top panel) are all compatible within statistical errors, showing no significant temperature dependence for the detection efficiency. Moreover, results in the bottom panel indicate how NUV-HD3 devices reach a PDE saturation at lower values of OV (at $V_{OV} \sim 4$ V) with respect to HD1 SiPMs (saturating at $V_{OV} \sim 6 - 7$ V).

The dependence of the cross-talk probability p on the SiPM over-voltage is shown in Figure 15. As expected, p increases with the applied bias voltage, reflecting the larger number of secondary photons produced by the avalanche. For HD3 SiPMs $p = (30 \pm 4)\%$ at $V_{OV} \sim 5$ V and T = 10°C, increasing by $(5.5 \pm 0.4)\%$/V. Measurements performed at different temperatures displayed in the top panel are compatible with each other within statistical errors, showing no significant temperature de-

pendence of the cross-talk probability. Results in the bottom panel indicate that HD1 devices exhibit slightly lower CT probability at the same over-voltage, even though values are compatible within statistical errors. The CT probability for HD1 SiPMs amounts to $p = (19 \pm 7)\%$ at $V_{OV} \sim 5$ V and T = 10°C, increasing by $(5.7 \pm 0.7)\%$/V. This value matches the HD3 one within the error.

3.3. Recovery time

Waveforms collected for each value of the over-voltage allowed us to estimate the recovery time of the fired cell. In order to get rid of the signal's long tail and of the afterpulse contribution, we first filtered the waveforms applying the "differential leading edge discriminator" (DLED) method developed by [28]. In this algorithm, a delayed copy of the signal is inverted and then subtracted to the original waveform. We used the filtered waveforms only to select those events without any afterpulses or dark counts occurring in the tail time window (i.e. 700 ns after the signal onset). We repeated the multi-gaussian fitting procedure on the 30-ns charge distribution of the selected waveforms and identified those corresponding to the single photo-electron.

The selected single photo-electron events were then used to calculate an average single p.e. waveform, which is shown in Figure 16 for T = 10°C and $V_{OV} = 4.9$ V. The shaded area indicates the standard deviation calculated for each data point. We note that the average waveform shows a small dip right before the signal onset, which is due to an external noise induced by the trigger signal and which we could not completely eliminate. We then fitted the average waveform $\bar{v}_{Ampl}$ in an interval of 485 ns, starting 50 ns after the signal onset, with a simple exponential in the form:

$$\bar{v}_{Ampl} = A_{rec} \cdot e^{-t/\tau_{rec}}, \quad (5)$$

where A_{rec} is a normalization constant and τ_{rec} represents the recovery time of the fired cell. Here $\tau_{rec} = (194 \pm 6)$ ns. In order to investigate possible dependencies on the fitting procedure, we considered different fit ranges. The starting point was kept fixed at 50 ns after the signal onset, while the fit range was changed between 135 and 585 ns, in steps of 50 ns. We see that the fit provides stable results if the fit range is larger than ~ 300 ns, i.e. once all the tail of the signal is taken into account and the waveform is back to the baseline level. Therefore, all results are quoted for a fit range of 485 ns.

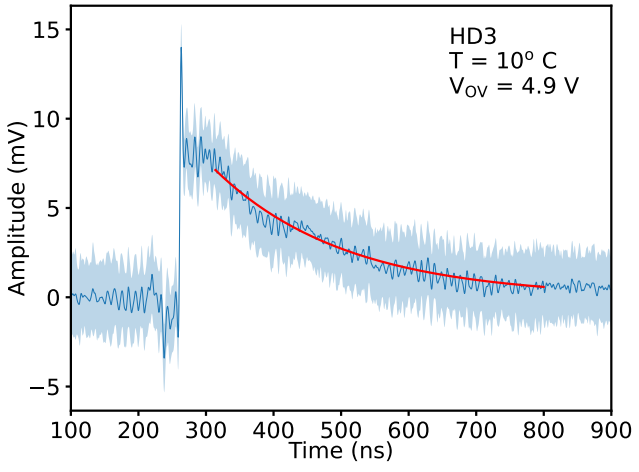

Figure 16: Average waveform obtained from all waveforms corresponding to the single p.e., collected at T = 10°C and $V_{OV} = 4.9$ V. An exponential fit (red solid line) is superimposed on the average waveform.

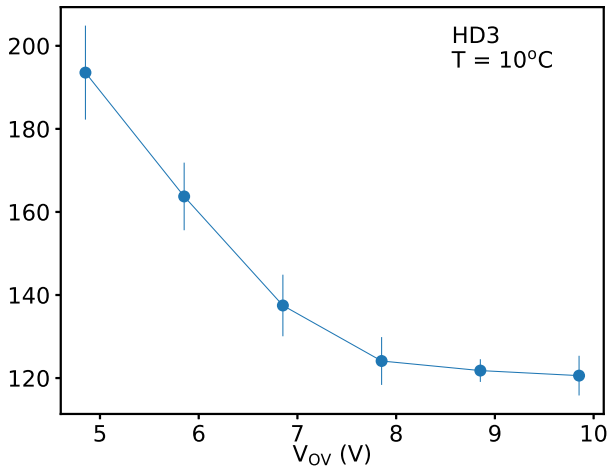

Figure 17: Recovery time for the HD3 SiPM as a function of the applied over-voltage at a fixed temperature T = 10°C.

Figure 17 presents the recovery time of the HD3 SiPM as a function of the applied over-voltage. τ_{rec} decreases from a value of ~ 190 ns to a minimum of ~ 120 ns in the explored OV range. This dependence might be ascribed to a non-constant microcell capacitance value with increasing OV, as already mentioned in section 3.1. Anyway, we point out that the recovery time cannot be directly correlated with the quenching resistor R_q and the juction capacitance of the microcell, since it depends also on the parasitic grid capacitance of the SiPM and on the input resistance of the readout circuit (see [24, 29]). This latter contribution can be neglected for small-sized SiPMs, while it is not marginal for the SiPMs studied in this work, given their relatively large dimension.

3.4. Dark count rate

In order to measure random dark counts and pulses responsible for the dark count rate of the devices, we acquired waveforms under dark conditions. A passive shaping network was added to the readout electronics right after the gain stage, in order to avoid pile-up effects of the signals which may occur due to their long tails. This precaution simplifies the offline analysis, leading to more reliable results. In order to increase the statistics, waveforms were acquired over a much longer time window of 1 ms. We studied the DCR dependence with temperature in a wide range between T = −20°C and T = 30°C.

For each run we selected pulses exceeding a threshold set at approximately half the amplitude of the single photo-electron, obtaining the arrival time and amplitude of each pulse, and the

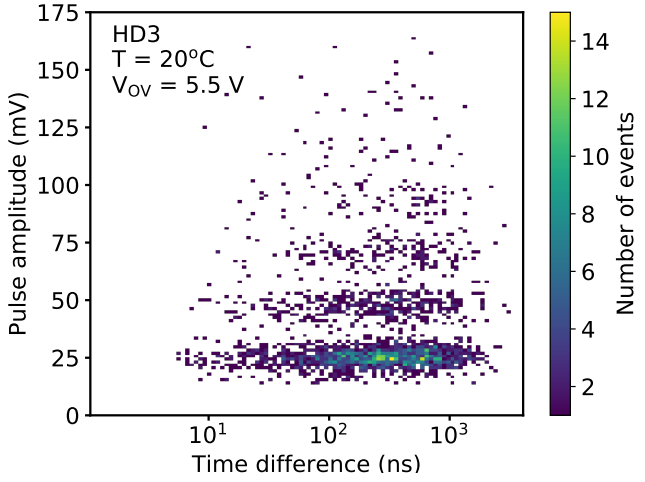

Figure 18: Density plot of the pulse amplitude in mV versus the time distance in ns between consecutive peaks measured at T = 20°C and V_{OV} = 5.5 V for the HD3 SiPM. Lighter colours indicate regions with a higher number of events.

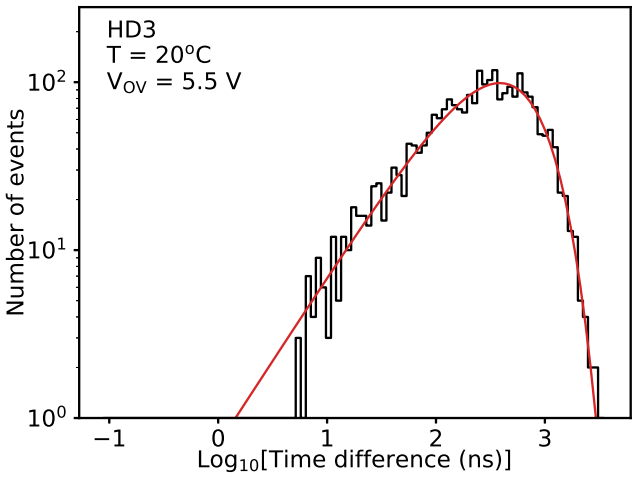

Figure 20: Distribution of the logarithm of the time difference between successive pulses measured at T = 20°C and V_{OV} = 5.5 V for HD3 devices.

time difference to the following one. Figure 18 shows the density plot of the pulse amplitude versus the time distance between successive pulses, plotted in logarithmic time-difference bins, at T = 20°C and V_{OV} = 5.5 V. The various groups of dark events with approximately equal pulse amplitude correspond to one, two, three, ..., i fired microcells, respectively. A similar representation of the spectrum from dark counts is given in Figure 19 showing the first three peaks of the dark pulse amplitude distribution fitted with a multi-gaussian function of the form of Equation 3 (red curve).

The temporal information regarding the arrival time of different dark pulses allows us to estimate the dark count rate. Due to Poisson statistics, the distribution of the time difference Δt between two consecutive dark pulses follows an exponential of the form $\propto e^{-(\Delta t \cdot DCR)}$ [21, 30]. The distribution of time delays

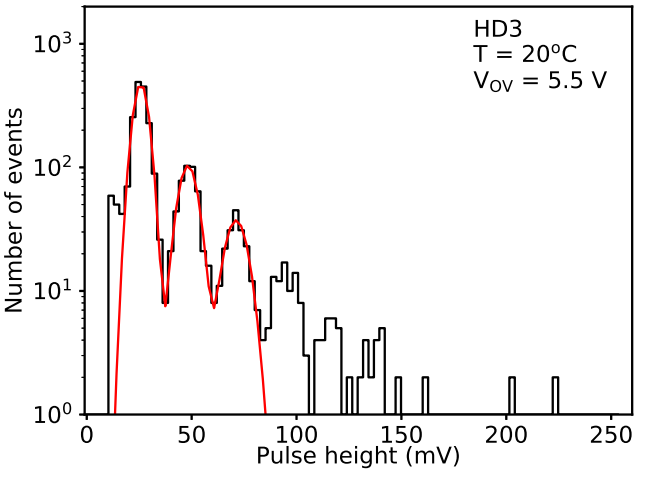

Figure 19: Distribution of the dark pulse amplitudes measured at T = 20°C and V_{OV} = 5.5 V for the HD3 SiPM. A multi-gaussian fit of the first three peaks is superimposed to the data (red curve).

for random dark counts can be expressed as

$$\frac{dN}{d(\log_{10}(\Delta t))} = A \cdot \Delta t \cdot e^{-\Delta t/\tau} = A \cdot \Delta t \cdot e^{-DCR \cdot \Delta t}, \qquad (6)$$

where A is a normalization constant and $\tau = \Delta t_{max} = 1/DCR$ represents the time at which the function reaches its maximum value. The distribution of the logarithm of the time delay between consecutive pulses, $\log_{10}(\Delta t)$, is shown in Figure 20, where the superimposed red curve is the best fit given by equation 6 with $DCR = (2.6 \pm 0.1)$ MHz.

We performed the same analysis procedure for the whole set of temperatures previously discussed and evaluated the DCR evolution as a function of the applied over-voltage. Results are presented in the top panel of Figure 21. The DCR exhibits a strong dependence from the temperature, as expected, increasing from ~ 160 kHz at T = −20°C to ~ 5 MHz at T = 30°C (for V_{OV} ~ 5 V). We applied an exponential function to the DCR values in the form:

$$DCR = B \cdot e^{bV_{OV}}, \qquad (7)$$

where B is a normalization factor strongly dependent on the temperature, ranging from ~ 60 kHz at T = −20°C to ~ 3 MHz at T = 30°C, and b represents the exponential coefficient, which remains almost constant within the error at all temperatures (b ~ 0.15/V).

A comparison of the DCR values as a function of the applied over-voltage for the HD1 and HD3 SiPMs at a fixed temperature T = 20°C is given in the bottom panel of Figure 21. At the same OV, HD1 SiPMs display a slightly smaller DCR than HD3 SiPMs, e.g. $DCR_{HD1} = 2.1 \pm 0.1$ MHz at V_{OV} ~ 5 V. This is attributed to the smaller cell size (30 μm vs 40 μm) which leads to a smaller fill factor.

An equivalent representation of the temperature dependence of the DCR for the HD3 SiPM is given in Figure 22, showing the DCR evolution as a function of the temperature in a range of

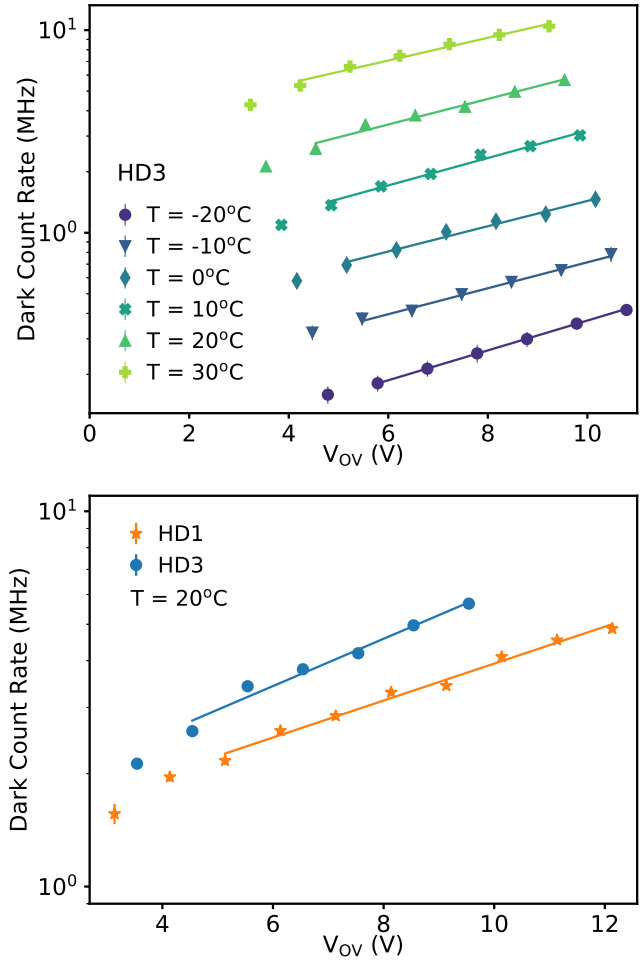

Figure 21: DCR as a function of the applied over-voltage for the HD3 SiPM at different temperatures (top panel) and for the HD1 and HD3 SiPM at T = 20°C (bottom panel).

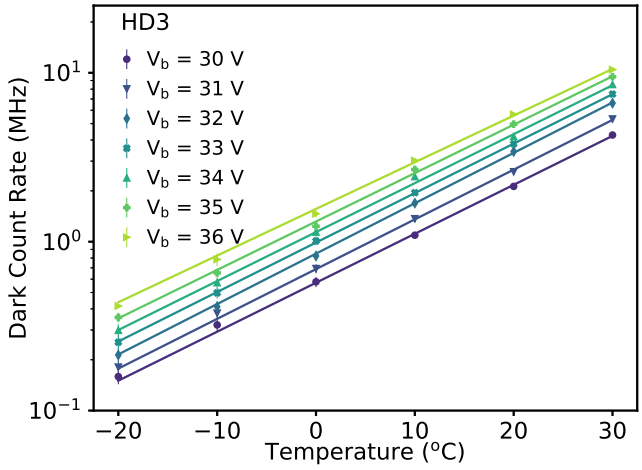

Figure 22: DCR as a function of the temperature for different bias voltages. Data were fitted with an exponential function.

bias voltages between 30 and 36 V. We applied an exponential function to the DCR values in the form

$$DCR = C \cdot e^{cT} . \tag{8}$$

where C is a normalization factor increasing from $\sim$ 0.6 MHz at V_b = 30 V to $\sim$ 1.6 MHz at V_b = 36 V, and c represents the exponential coefficient, which is independent of the bias voltage ($c \sim 0.07/°C$).

4. PDE measurements

The PDE is defined as the probability that a SiPM detects an incoming photon. It can be expressed as the number of photon-discharged microcells (N_F) divided by the number of incident photons (N_I):

$$PDE = \frac{N_F}{N_I}. \tag{9}$$

In general, at a given temperature, the PDE is a function of the bias voltage V_b and the incident photon wavelength λ, and it is usually expressed as the factorization of three quantities: the Quantum Efficiency $QE(\lambda)$, i.e. the probability for an incident photon to create an electron-hole pair, the avalanche initiation probability $\eta(V_b)$, i.e. the probability for a primary carrier to trigger an avalanche in the cell, and the fill factor of the device ϵ_g [31], which takes into account the probability for an electron-hole pair to be created in a position in the depletion layer from which a carrier can reach the high electric field region:

$$PDE(V_b, \lambda) = QE(\lambda) \cdot \eta(V_b) \cdot \epsilon_g . \tag{10}$$

We determined the PDE of HD3 SiPMs as a function of the applied over-voltage, the wavelength, and the incident photon angle, according to the procedures described below. All the measurements were performed in a dark box at a room temperature of T = 20°C.

4.1. PDE versus wavelength measurement

In order to perform PDE measurements as a function of the wavelength we followed the procedure described in [32]. The layout of the experimental setup is shown in Figure 23. We employed a Xenon lamp as continuous light source, which emits in a range from 250 nm to 2700 nm, in combination with an Andover optical band-pass filter, which is needed to select a 10-nm band around different wavelengths at 50% transmission. The light was guided by means of an optical fiber through the 90°

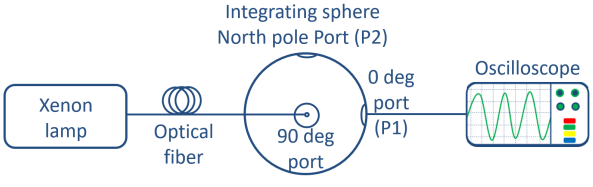

Figure 23: Scheme of the PDE measurement setup.

Figure 24: Picture of the integrating sphere, showing the entry port (90°) and the two exit ports, P1 (0°) and P2 (North pole), all oriented perpendicular to each other.

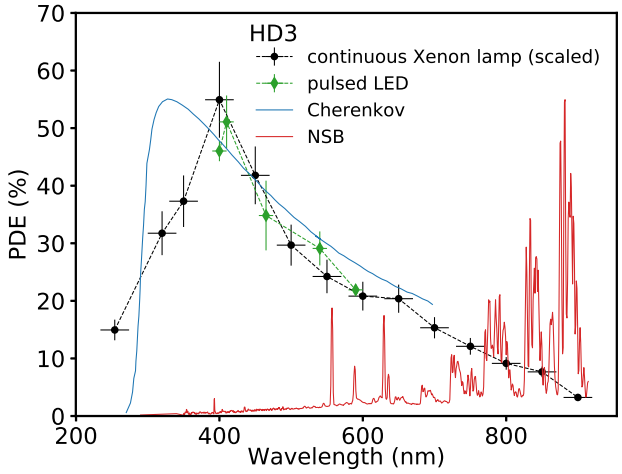

Figure 25: PDE for the HD3 SiPM measured as a function of the photon wavelength at an over-voltage of 5.5 V, using the Xenon lamp (black data points) and using the LEDs (green data points). The Cherenkov spectrum (blue line) and the night sky background (NSB, taken from [33]) under dark conditions (red line) are also shown.

port of an integrating sphere Newport 819D, which is shown in Figure 24. The whole setup was placed inside a dark box in order to isolate it from all possible light sources that could interfere with the SiPM light detection. Data were acquired using a Teledyne Lecroy HDO9494 High-Definition Oscilloscope and a different readout electronics with respect to the one used in Section 3. All measurements were performed at $V_{OV} = 5.5$ V. We note that this procedure does not allow us to differentiate cross-talk, afterpulse and dark pulses contributions, thus the PDE value will be overestimated with respect to the one determined under pulsed light conditions (described later in this Section).

We placed the HD3 SiPM in front of the 0° port (hereafter P1 port) of the integrating sphere, and positioned a calibrated PMT Hamamatsu R9880U-01 at the North pole port (hereafter P2 port), in order to determine the optical power. The PMT signal was read out using the oscilloscope.

In order to compensate for possible differences of the signal amplitude measured at different ports (P1 and P2) of the integrating sphere, we first placed the PMT at both positions and determined a calibration factor R given by $R = V_2/V_1$, where V_1 and V_2 are the signals amplitudes measured by the PMT at the P1 and P2 ports, respectively. Such a correction is particularly needed when a diaphragm is placed in front of the SiPM in order to reduce the amount of incident light and to make sure that the light spot is smaller than the SiPM's sensitive area. We note that the calibration ratio R determined experimentally strongly depends on the wavelength of the impinging radiation. The values obtained for R partially compensate for the difference in sensitivity between the PMT and the SiPM, since the SiPM benefits from a higher gain.

In order to achieve the best possible conditions for optimally operating both the SiPM and the PMT, we conveniently adjusted the diaphragm aperture and moved the support of the SiPM along the transverse directions until the signal amplitude observed was maximal.

We derived the absolute PDE as a function of the wavelength of the incident radiation following the photo-current method presented in [32]:

$$PDE(\lambda) = \frac{I_{\mathrm{SiPM}} \cdot R \cdot h\nu}{q_e \cdot G' \cdot P_{\mathrm{opt}}}, \qquad (11)$$

where I_{SiPM} is the SiPM output current, obtained by first dividing the measured voltage by the oscilloscope impedance (50 Ω) and then subtracting the SiPM output current obtained in dark conditions; R is the calibration ratio, G' is the gain of the system (including the front-end amplifier gain) at the operating point, ν is the frequency of the incident radiation, h is the Planck constant, and P_{opt} is the incident optical power measured with the calibrated PMT mounted onto the P2 port behind the diaphragm. We derived the gain from the amplitude spectrum obtained using pulsed LED light at 410 nm at the same over-voltage used for the measurements. We note that this is a distinct quantity with respect to the gain values presented in Section 3.1. The PDE's uncertainty is calculated by means of error propagation taking into account the corresponding errors of all measured quantities. The uncertainties of the gain and QE of the PMT are neglected.

As already stated, these measurements overestimate the PDE, since they include the contribution from the correlated noise. Therefore, we should refer to this quantity as relative PDE. The absolute scale of the PDE can be then obtained by dividing the measurements by the Excess Charge Factor (in-ECF), which can be estimated as $(1 + CT)$ [27, 34], being CT the cross-talk value reported in Figure 15.

Figure 25 shows the relative PDE as a function of the wavelength in the range 254–900 nm obtained using the Xenon lamp, calculated through Equation (11) and normalized by the factor $(1 + CT)$ (black data points). The uncertainty on the PDE data points include the error on the CT (taken from Fig. 15).

In order to determine the absolute PDE, we repeated our measurements as a function of the wavelength with a set of pulsed LED sources emitting at 400, 410, 465, 540, and 590 nm. Details of this method are reported in Section 4.2. Results are presented in Figure 25 as green points. It is worth noting that results obtained with the two methods are in general agreement, suggesting that the normalized relative PDE well

reproduces the PDE dependence on the wavelength. Results at 400 and 410 nm show a non-smooth variation, which can be ascribed to oscillations in the PDE due to interference caused by the thin passivation layer and by the lack of a coating on top of the SiPM, similarly to what is reported in [15, 21].

4.2. Absolute PDE measurement

The layout of the experimental setup used to measure the PDE as a function of the applied over-voltage is the same described in Section 4.1 and shown in Figure 23. The LED flasher is driven by an Agilent 33250 in a pulse mode to produce a 40 ns pulse width with a 1 kHz pulse frequency. We employed the calibrated PMT again in order to determine the correct power ratio, which is wavelength dependent. We used in turn LEDs with fixed wavelengths of 400, 410, 465, 510, and 590 nm.

Following the pulsed-light counting method described in [35], the PDE is determined by the ratio between the number of photons recorded by the SiPM, $n_{\rm pe}$, and the number of incident photons at the SiPM position, $n_{\rm inc,SiPM}$. This latter value is obtained from the number of incident photons on the calibrated PMT placed in front of the P2 port of the integrating sphere, $n_{\rm inc,PMT}$, divided by the calibration ratio R:

$$PDE = \frac{n_{\rm pe}}{n_{\rm inc,\,SiPM}} = R \cdot \frac{n_{\rm pe}}{n_{\rm inc,PMT}}. \tag{12}$$

As explained in Sections 3.1 and 3.2, both the amplitude and the charge distribution of the SiPM signal are connected to the number of observed photo-electrons, distributed according to a Poisson law, which is affected by cross-talk and afterpulses. However, the area of the first peak is unaffected by the correlated noise events. Indeed, the area of the first peak is proportional to the number of events, $N_{\rm ped}$, in which no photons have been detected. Following the prescription in [32], we used $N_{\rm ped}$ to estimate the PDE without any bias from the correlated noise effects. The number $n_{\rm pe}$ of detected photons can be determined from N_{ped} using the relation:

$$\begin{aligned} P(0, n_{\rm pe}) &= e^{-n_{\rm pe}} \\ \Rightarrow n_{\rm pe} &= -\ln\left(P(0, n_{\rm pe})\right) \\ &= -\ln\left(\frac{N_{\rm ped}}{N_{\rm tot}}\right) + \ln\left(\frac{N_{\rm ped}^{\rm dark}}{N_{\rm tot}^{\rm dark}}\right), \end{aligned} \tag{13}$$

where $P(0, n_{\rm pe})$ is the probability to detect 0 photons given by a Poisson distribution with mean value $n_{\rm pe}$, $N_{\rm ped}^{\rm dark}$ is the number of pedestal events in the spectrum obtained in the absence of light pulses, and $N_{\rm tot}$ and $N_{\rm tot}^{\rm dark}$ are the total number of events in the laser-induced and dark spectrum, ($\sim$ 20000 events).

We calculated $N_{\rm ped}$ and $N_{\rm ped}^{\rm dark}$ by fitting the pedestal peak of the charge distribution (in a 40 ns time window) with a Gaussian function and integrating it around the mean value in an interval of $\pm\,3\,\sigma$ in light and dark conditions, respectively. The number of photons incident on the PMT was calculated by integrating the mean PMT signal $U(t)$ measured with the oscilloscope, and by dividing this number by the oscilloscope impedance (50 Ω),

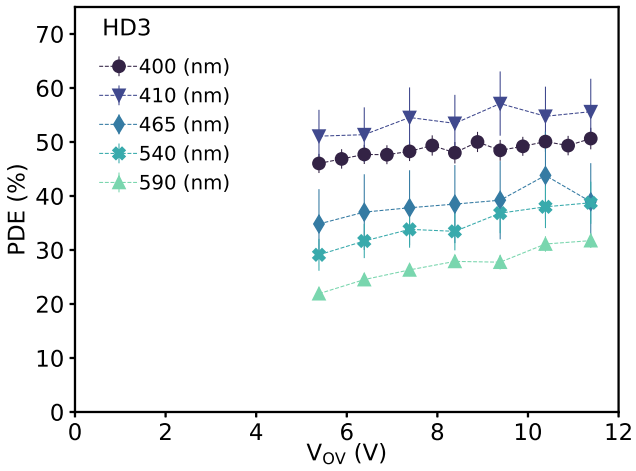

Figure 26: PDE as a function of the applied over-voltage for the HD3 SiPM, measured at different wavelengths from 400 nm to 590 nm. The dashed lines only connect experimental data and do not represent an analytical fit.

the electron charge, the gain G and the quantum efficiency QE of the PMT:

$$n_{\rm PMT} = \frac{1}{50\Omega \cdot q_e \cdot G \cdot QE} \int U(t)dt. \tag{14}$$

We extracted the last two numbers from the PMT reference table for the correspondent power supply (at 700 V the QE is 22% and the gain is $2 \cdot 10^5$). The calibration ratio R is obtained from the ratio between the area in the P1 and in the P2 ports. Finally, the PDE was calculated according to Equation (12) at different bias voltages. Results are presented in Figure 26 for different wavelengths of the LED flasher.

The NUV-HD3 SiPM exhibits maximum values at wavelengths around 410 nm, in agreement with what we previously derived with a continuous wave source (see Figure 25 for comparison). Moreover, we note that for short wavelengths the PDE saturates above 4 V of OV, thus providing a confirmation of the results shown in the top panel of Figure 14. For longer wavelengths the saturation occurs at higher OV values. This is due to the fact that longer wavelengths penetrate deeper in the p-n junction, where the avalanche is triggered by the holes, which reach saturation for higher OV values [36].

4.3. Angle-dependent PDE measurements

Finally, we measured the response of the SiPM as a function of the angle of incidence. The experimental setup consists of a set of pulsed LED flashers with wavelengths ranging from 410 nm to 880 nm, placed inside the integrating sphere. In order to take measurements at different incidence angles of the light, we placed the SiPM and its front-end board on a rotary stage (Thorlabs PRMTZ8/M), as shown in Figure 27.

We varied the angle of incidence starting from 0°, i.e. placing the axis of the light beam direction perpendicular to the SiPM surface, up to 80°, where the light beam direction is almost parallel to the SiPM surface. Angle variation was set in steps of 10°. The LED light source was placed in an integrating sphere which acted as a diffusor. The light was guided by

an optical fibre to the SiPM, mounted behind a collimator. We acquired the amplified output signal of the SiPM by means of the same oscilloscope used in Sections 4.1 and 4.2. From the charge spectrum, we evaluated the number of photons detected at each angle of incidence of the light as we did in the previous Section, using Equation (13). Results of all measurements performed in a wavelength range from 410 nm to 880 nm are reported in the top panel of Figure 28. The absolute PDE measured values were normalized to a cosine law in order to take into account the projection of the light beam on the detector's surface.

We then normalized the PDE measurements to the value obtained at $\Theta = 0°$ and report them in the bottom panel of Figure 28. It can be noted that PDE values do not show a strong dependence on the incident angle and decrease by less than 20% for angles smaller than 60°, with the exception of the longest wavelength (880 nm). We point out that we did not take into account possible losses induced by Fresnel reflections on the SiPM surface. These could explain the deviation from the cosine dependence observed at the longest wavelength and at incident angles above 60° (see for example [37]), while we prove that they are negligible with respect to statistical errors for wavelengths < 600 nm.

5. Conclusions

In this work we focused on the characterization of devices specifically designed for astroparticle physics applications. Recent developments of SiPM technologies led to an improvement of their performances in the NUV domain, making these devices mature and suitable for Cherenkov light detection. As proven by FACT's long-term stability and observations performed with strong moon light, SiPMs can safely be operated under bright light conditions, thus allowing a significant increase in the Cherenkov telescopes duty cycle [38, 39, 40].

A long-term synergy work between FBK and INFN led to the recent development of an *ad-hoc* research line of highly sensitive photon detectors dedicated to Cherenkov light detection. Different technologies and designs have been implemented over the years in order to improve the NUV SiPM technology. Major advancements include the optimization of the active high-field region, with the aim of increasing the avalanche triggering probability and the PDE. Many SiPM generations of the NUV-HD technology were tested since 2016 at the INFN laboratories leading to the optimization of the devices for CTA applications.

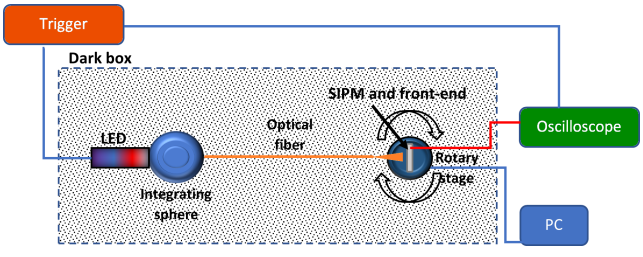

Figure 27: Scheme of the set-up used for angle-depenedent PDE measurements.

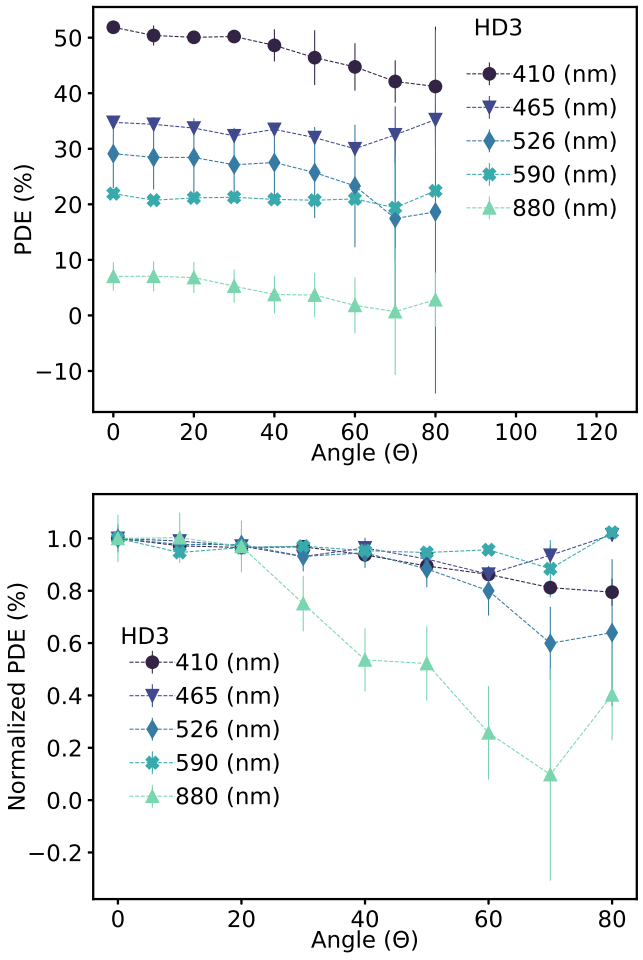

Figure 28: PDE (top panel) and PDE normalized to its highest value (bottom panel) for the HD3 SiPM as a function of the radiation's incident angle, ranging from 0° to 80°. Wavelengths range from 410 nm to 880 nm. The dashed lines only connect experimental data and do not represent an analytical fit.

In this work, we presented a full characterization of a specific SiPM produced by FBK which has been chosen to equip the pSCT camera [8]. Devices with a 6×6 mm^2 area and 40 μm cell pitch, labelled as HD3, were tested and their performance was compared with devices of a previous generation (HD1). All results obtained prove the excellent performance of the device in terms of gain, cross-talk probability, PDE, and SNR, and are summarized in Table 2. We point out that independent measurements previously conducted on devices with the same HD3 technology and a smaller 1×1 mm^2 area [25, 41] provide consistent results with the ones presented in this work in terms of the properties of the individual microcell, i.e. gain, CT and PDE.

In Section 1, we discussed the many benefits of SiPMs over PMTs including their much lower operating voltage, the lower production costs, insensitivity to magnetic fields, and possibility to operate them also in partial moonlight, thus significantly increasing the duty cycle. Here we discuss in detail how the FBK NUV-HD technology satisfies CTA's main requirements [3]:

Table 2: Main characteristics of the FBK NUV-HD3 SiPM device chosen to equip the camera of pSCT, tested in this work.

V_{BD} (T = 25°C)	(26.49 ± 0.02) V
Change in V_{BD} with T	(31.1 ± 0.5) mV/°C
R_q (T = 25°C)	(1.11 ± 0.01) MΩ
Change in R_q with T	(−10.2 ± 0.4) kΩ/°C
I_s (T = 25°C)	(32 ± 9) pA
Gain (V_{OV} ∼ 5 V, T = 10°C)	$(4.01 \pm 0.02) \cdot 10^6$
Change in gain with OV	$(7.0 \pm 0.1) \cdot 10^5$/V
SNR (V_{OV} ∼ 5 V, T = 10°C)	9.08 ± 0.24
Saturation of detected photons	$V_{OV} \geq 5$ V
p (V_{OV} ∼ 5 V, T = 10°C)	(30 ± 4)%
Change in p with OV	(5.5 ± 0.4)%/V
τ_{rec} (V_{OV} ∼ 5 V, T = 10°C)	(194 ± 6) ns
DCR (V_{OV} ∼ 5 V, T = 20°C)	(2.6 ± 0.1) MHz
PDE (400 nm, V_{OV} ∼ 5 V, T = 20°C)	(55 ± 7)%

- **Spectral sensitivity –** In Figure 25 we showed that the peak of the NUV-HD3 response lies within 50 nm of the peak of the Cherenkov light spectrum, which is cut off below 300 nm due to atmospheric transmission effects and falls off towards longer wavelengths as $1/\lambda$. The FBK NUV-HD3 device reaches a peak PDE of (55 ± 7)% at ∼400 nm and does not fall under ∼ 20% up to wavelengths of about 650 nm, as requested by CTA. In general, SiPMs show higher sensitivities with respect to current PMT devices at wavelengths $\gtrsim$ 600 nm, where the NSB is more relevant. However, this effect can be easily mitigated with appropriate optical windows placed in front of the telescope focal plane, which are optimized to filter out long wavelengths and reduce the background rate due to the NSB.

- **Sensor area –** The Medium Size Telescopes for CTA in single mirror optics are required to have a sensor dimension of 50 mm, corresponding to a pixel size of 0.18°. In the case of a secondary-optics design, as proposed for SCT, a consequently smaller angular pixel size of 0.07° is achieved, corresponding to a physical size of 6 mm. Thus, the NUV-HD3 SiPM devices presented in this work have been developed accordingly to this requirement.

- **Dynamic range and linearity –** As shown in this work, 6×6 mm^2 NUV-HD3 SiPMs proved to be able to detected light down to the single photon. Having a cell pitch of 40 μm, they also provide a very large number of micro-cells ($N_{pix} \approx 22500$), thus yielding a dynamic range way higher than the requested 5,000 photo-electrons. The linearity of the SiPM response and the dynamic range do depend also on the read-out electronics chosen to equip the camera. The detailed study of these features for the specific CTA application will be performed in dedicated works.

- **Temporal response –** Cherenkov light flashes produced in the atmosphere are ∼ 10 − 15 ns long, with a leading edge of ∼ 2 − 3 ns, and the time dispersion of Cherenkov photons across a camera image is of the order of the nanosecond, depending on the energy of the primary particle. Indeed, it becomes crucial for the signal produced by the chosen photo-sensors to preserve the time structure, and in particular the rising edge, of the Cherenkov light pulse. In Figure 9 we showed a collection of waveforms acquired with the NUV-HD3 devices. We note that in general the leading edge rise time is almost instantaneous, driven by the charge multiplication duration. In the end, the main limiting factor is given by the characteristics of the read-out electronics and of the measuring instrument. A detailed investigation of the FBK SiPM rise times can be found in [42], and is found to be ∼ 120 ps, satisfying the sub-nanosecond resolution at sensor level. Still, the time resolution of the full chain to be implemented in CTA applications should take into account the read-out electronics, which goes beyond the scope of this paper.

We conclude that the devices presented in this work, which are the product of many years of iterative improvements in a constant synergy between INFN and FBK, nicely match the criteria for photo-detectors required by the CTA project listed in [3], which actually represented general guidelines for the development of various types of sensors (both PMTs and SiPMs) in the following years.

The FBK NUV-HD3 presented in this work were assembled in 16 pixels arrays in the camera of the pSCT telescope [8]. They were successfully installed on the first sector of the pSCT camera in 2018. More details regarding the performance of these devices arranged in arrays developed at the INFN laboratories and to their sample-to-sample performance variations are reported in a dedicated publication [43]. As discussed in [8] and [11], the commissioning phase of the pSCT showed very encouraging results, representing an important milestone in the project development.

Acknowledgments

This research was supported by grants from the Istituto Nazionale di Fisica Nucleare (INFN) in Italy and the U.S. National Science Foundation and the Smithsonian Institution in the USA. The authors gratefully acknowledge the Italian National Grant TECHE.it funded by the Italian Ministry of Education. The authors also ackowledge A. Gola, G. Paternoster and G. Borghi of Fondazione Bruno Kessler for many fruitful discussions and collaboration. L.D. ackowledges the

initiative “Research for Innovation (REFIN) - codice progetto 73A60A91” financed by Regione Puglia, Italy.

References

[1] H. Anderhub, M. Backes, A. Biland, et al., FACT—The first Cherenkov telescope using a G-APD camera for TeV gamma-ray astronomy, Nuclear Instruments and Methods in Physics Research Section A: Accelerators, Spectrometers, Detectors and Associated Equipment 639 (1) (2011) 58 – 61. doi:https://doi.org/10.1016/j.nima.2010.10.081.

[2] D. Dorner, A. Arbet-Engels, D. Baack, et al., FACT - Highlights from more than Seven Years of Unbiased Monitoring at TeV Energies, in: Proceedings of 36th International Cosmic Ray Conference, PoS(ICRC2019), Vol. 358, 2019, p. 665. doi:10.22323/1.358.0665.

[3] M. Actis, G. Agnetta, F. Aharonian, et al., Design concepts for the Cherenkov Telescope Array CTA: an advanced facility for ground-based high-energy gamma-ray astronomy, Experimental Astronomy 32 (2011) 193–316. doi:10.1007/s10686-011-9247-0.

[4] Cherenkov Telescope Array Consortium, B. S. Acharya, I. Agudo, et al., Science with the Cherenkov Telescope Array, World Scientific, 2019. doi:10.1142/10986.

[5] G. Ambrosi, M. Ambrosio, C. Aramo, et al., INFN Camera demonstrator for the Cherenkov Telescope Array, in: The 34th International Cosmic Ray Conference (ICRC2015), Vol. 236 of Proceedings of Science, 2016, p. 956. doi:10.22323/1.236.0956.

[6] K. Byrum, B. Humensky, W. Benbow, et al., A Medium Sized Schwarzschild-Couder Cherenkov Telescope Mechanical Design Proposed for the Cherenkov Telescope Array, in: The 34th International Cosmic Ray Conference (ICRC2015), Vol. 236 of Proceedings of Science, 2016, p. 1029. doi:10.22323/1.236.1029.

[7] G. Ambrosi, M. Ambrosio, C. Aramo, et al., An upgrade of the camera focal plane of a Schwarzschild-Couder Telescope prototype (pSCT) for the Cherenkov Telescope Array (CTA), in: ”New eyes on the Universe” CRIS 2016 - Proceedings of the Cosmic Rays International Seminars, Vol. 291 of Nuclear and Particle Physics Proceedings, 2017, pp. 48–51. doi:10.1016/j.nuclphysbps.2017.06.011.

[8] C. B. Adams, G. Ambrosi, M. Ambrosio, et al., Design and performance of the prototype Schwarzschild-Couder telescope camera , Journal of Astronomical Telescopes, Instruments, and Systems 8 (1) (2022) 1 – 38. doi:10.1117/1.JATIS.8.1.014007.

[9] C. Adams, G. Ambrosi, M. Ambrosio, et al., Characterization and assembly of near-ultraviolet SiPMs for the Schwarzschild-Couder medium-size telescope proposed for the CTA Observatory, in: R. B. James, A. Burger, S. A. Payne (Eds.), Hard X-Ray, Gamma-Ray, and Neutron Detector Physics XXI, Vol. 11114, International Society for Optics and Photonics, SPIE, 2019, pp. 52 – 60. doi:10.1117/12.2530617.

[10] C. Adams, G. Ambrosi, M. Ambrosio, et al., Development and operations of INFN optical modules for the SCT Telescope camera proposed for the Cherenkov Telescope Array Observatory, in: Proceedings of 36th International Cosmic Ray Conference — PoS(ICRC2019), Vol. 358, 2019, p. 810. doi:10.22323/1.358.0810.

[11] C. B. Adams, R. Alfaro, G. Ambrosi, et al., Detection of the Crab Nebula with the 9.7 m prototype Schwarzschild-Couder telescope, Astroparticle Physics 128 (2021) 102562. arXiv:2012.08448, doi:10.1016/j.astropartphys.2021.102562.

[12] C. Piemonte, R. Battiston, M. Boscardin, et al., Characterization of the First Prototypes of Silicon Photomultiplier Fabricated at ITC-irst, IEEE Transactions on Nuclear Science 54 (1) (2007) 236–244. doi:10.1109/TNS.2006.887115.

[13] C. Piemonte, A. Ferri, A. Gola, et al., Development of an automatic procedure for the characterization of silicon photomultipliers, in: 2012 IEEE Nuclear Science Symposium and Medical Imaging Conference Record (NSS/MIC), 2012, pp. 428–432. doi:10.1109/NSSMIC.2012.6551141.

[14] C. Piemonte, A. Ferri, A. G. and, Characterization of the first FBK High-Density Cell Silicon Photomultiplier Technology, IEEE Transactions on Electron Devices 60 (8) (2013) 2567–2573. doi:10.1109/TED.2013.2266797.

[15] T. Pro, A. Ferri, A. Gola, et al., New Developments of Near-UV SiPMs at FBK, IEEE Transactions on Nuclear Science 60 (3) (2013) 2247–2253. doi:10.1109/TNS.2013.2259505.

[16] F. Acerbi, A. Ferri, G. Zappala, et al., NUV Silicon Photomultipliers With High Detection Efficiency and Reduced Delayed Correlated-Noise, IEEE Transactions on Nuclear Science 62 (3) (2015) 1318–1325. doi:10.1109/TNS.2015.2424676.

[17] F. Acerbi, A. Ferri, G. Zappala, et al., Technological and design improvements of FBK NUV silicon-photomultipliers, in: 2015 Fotonica AEIT Italian Conference on Photonics Technologies, 2015, pp. 1–3. doi:10.1049/cp.2015.0150.

[18] C. Piemonte, F. Acerbi, A. Ferri, et al., Performance of NUV-HD Silicon Photomultiplier Technology, IEEE Transactions on Electron Devices 63 (3) (2016) 1111–1116. doi:{10.1109/TED.2016.2516641}.

[19] A. Gola, F. Acerbi, M. Capasso, et al., NUV-Sensitive Silicon Photomultiplier Technologies Developed at Fondazione Bruno Kessler, Sensors 19 (2). doi:10.3390/s19020308.

[20] G. Ambrosi, E. Bissaldi, N. Giglietto, et al., Silicon Photomultipliers and front-end electronics performance for Cherenkov Telescope Array camera development, Nuclear Instruments and Methods in Physics Research Section A: Accelerators, Spectrometers, Detectors and Associated Equipment 845 (2017) 8 – 11. doi:https://doi.org/10.1016/j.nima.2016.04.050.

[21] A. N. Otte, D. Garcia, T. Nguyen, D. Purushotham, Characterization of Three High Efficiency and Blue Sensitive Silicon Photomultipliers, Nucl. Instrum. Meth. A846 (2017) 106–125. doi:10.1016/j.nima.2016.09.053.

[22] C. Xu, Study of the Silicon Photomultipliers and Their Applications in Positron Emission Tomography, DESY Dissertation Database 013 (1) (2014) 1–129. doi:http://dx.doi.org/10.3204/DESY-2014-02771.

[23] Y. Musienko, A. Heering, R. Ruchti, M. Wayne, A. Karneyeu, V. Postoev, Radiation damage studies of silicon photomultipliers for the CMS HCAL phase I upgrade, in: Proceedings, 7th International Conference on New developments in photodetection (NDIP14): Tours, France, June 30-July 4, 2014, Vol. 787, 2015, pp. 319–322. doi:http://http://dx.doi.org/10.1016/j.nima.2015.01.012.

[24] F. Corsi, A. Dragone, C. Marzocca, et al., Modelling a silicon photomultiplier (SiPM) as a signal source for optimum front-end design, Nuclear Instruments and Methods in Physics Research Section A: Accelerators, Spectrometers, Detectors and Associated Equipment 572 (1) (2007) 416–418. doi:https://doi.org/10.1016/j.nima.2006.10.219.

[25] C. Adams, G. Ambrosi, M. Ambrosio, et al., Status of the development of NUV SiPMs for INFN optical modules for the SCT medium sized telescope proposed for the CTA observatory, Nuclear Instruments and Methods in Physics Research Section A: Accelerators, Spectrometers, Detectors and Associated Equipment 982 (2020) 164486. doi:https://doi.org/10.1016/j.nima.2020.164486.

[26] V. Chmill, E. Garutti, R. Klanner, M. Nitschke, J. Schwandt, Study of the breakdown voltage of SiPMs, Nuclear Instruments and Methods in Physics Research Section A: Accelerators, Spectrometers, Detectors and Associated Equipment 845 (2017) 56–59, proceedings of the Vienna Conference on Instrumentation 2016. doi:https://doi.org/10.1016/j.nima.2016.04.047.

[27] S. Vinogradov, T. Vinogradova, V. Shubin, et al., Probability distribution and noise factor of solid state photomultiplier signals with cross-talk and afterpulsing, in: 2009 IEEE Nuclear Science Symposium Conference Record (NSS/MIC), 2009, pp. 1496–1500. doi:10.1109/NSSMIC.2009.5402300.

[28] A. Gola, C. Piemonte, A. Tarolli, The DLED Algorithm for Timing Measurements on Large Area SiPMs Coupled to Scintillators, IEEE Transactions on Nuclear Science 59 (2) (2012) 358–365. doi:10.1109/TNS.2012.2187927.

[29] F. Licciulli, C. Marzocca, Parameter Extraction Method for the Electrical Model of a Silicon Photomultiplier, IEEE Transactions on Nuclear Science 63 (5) (2016) 2517–2526. doi:10.1109/TNS.2016.2594585.

[30] R. Klanner, Characterisation of SiPMs, Nuclear Instruments and Methods in Physics Research Section A: Accelerators, Spectrometers, Detectors and Associated Equipment 926 (2019) 36–56, silicon Photomultipliers: Technology, Characterisation and Applications. doi:https://doi.org/10.1016/j.nima.2018.11.083.

[31] F. Acerbi, S. Gundacker, Understanding and simulating SiPMs, Nuclear Instruments and Methods in Physics Research Section A: Accelerators, Spectrometers, Detectors and Associated Equipment 926 (2019) 16 – 35.

doi:https://doi.org/10.1016/j.nima.2018.11.118.

[32] P. Eckert, H.-C. Schultz-Coulon, W. Shen, et al., Characterisation studies of silicon photomultipliers, Nuclear Instruments and Methods in Physics Research A 620 (2-3) (2010) 217–226. doi:10.1016/j.nima.2010.03.169.

[33] C. Benn, S. Ellison, Brightness of the night sky over La Palma, New Astronomy Reviews 42 (6) (1998) 503–507. doi:https://doi.org/10.1016/S1387-6473(98)00062-1.
URL https://www.sciencedirect.com/science/article/pii/S1387647398000621

[34] S. Vinogradov, Analytical models of probability distribution and excess noise factor of solid state photomultiplier signals with crosstalk, Nuclear Instruments and Methods in Physics Research Section A: Accelerators, Spectrometers, Detectors and Associated Equipment 695 (2012) 247–251, new Developments in Photodetection NDIP11. doi:https://doi.org/10.1016/j.nima.2011.11.086.
URL https://www.sciencedirect.com/science/article/pii/S0168900211021565

[35] G. Zappalà, F. Acerbi, A. Ferri, et al., Set-up and methods for SiPM Photo-Detection Efficiency measurements, Journal of Instrumentation 11 (08) (2016) P08014–P08014. doi:10.1088/1748-0221/11/08/p08014.
URL https://doi.org/10.1088/1748-0221/11/08/p08014

[36] W. G. Oldham, R. R. Samuelson, P. Antognetti, Triggering phenomena in avalanche diodes, IEEE Transactions on Electron Devices 19 (9) (1972) 1056–1060. doi:10.1109/T-ED.1972.17544.

[37] M. Nemallapudi, S. Gundacker, A. Knapitsch, P. Lecoq, Z. Liu, E. Auffray, Sipm angular response and enhanced light extraction, IEEE Nuclear Science Symposium Conference Recorddoi:10.1109/NSSMIC.2013.6829586.

[38] A. Biland, T. Bretz, J. Buß, et al., Calibration and performance of the photon sensor response of FACT — the first G-APD Cherenkov telescope, Journal of Instrumentation 9 (10) (2014) P10012–P10012. doi:10.1088/1748-0221/9/10/p10012.

[39] T. Bretz, A. Biland, J. Buss, et al., FACT Threshold Prediction for Higher Duty Cycle and Improved Scheduling, in: International Cosmic Ray Conference, Vol. 33 of International Cosmic Ray Conference, 2013, p. 3024. arXiv:1308.1516.

[40] M. L. Knoetig, A. Biland, T. Bretz, et al., FACT Long-Term Stability and Observations during Strong Moon Light, in: International Cosmic Ray Conference, Vol. 33 of International Cosmic Ray Conference, 2013, p. 1132. arXiv:1307.6116.

[41] G. Ambrosi, M. Ambrosio, C. Aramo, et al., Characterization of FBK NUV-HD SiPMs for the pSCT camera proposed for the Cherenkov Telescope Array, Nuclear Instruments and Methods in Physics Research Section A: Accelerators, Spectrometers, Detectors and Associated Equipment 936 (2019) 542–544. doi:https://doi.org/10.1016/j.nima.2018.11.030.

[42] F. Acerbi, A. Ferri, A. Gola, N. Zorzi, C. Piemonte, Analysis of single-photon time resolution of FBK silicon photomultipliers, Nuclear Instruments and Methods in Physics Research Section A: Accelerators, Spectrometers, Detectors and Associated Equipment 787 (2015) 34–37, new Developments in Photodetection NDIP14. doi:https://doi.org/10.1016/j.nima.2014.10.057.
URL https://www.sciencedirect.com/science/article/pii/S0168900214012145

[43] G. Ambrosi, M. Ambrosio, C. Aramo, et al., Assembly and performance of SiPM arrays for the prototype SCT proposed for CTA, Nuclear Instruments and Methods in Physics Research Section A: Accelerators, Spectrometers, Detectors and Associated Equipment 1041 (2022) 167359. doi:https://doi.org/10.1016/j.nima.2022.167359.
URL https://www.sciencedirect.com/science/article/pii/S0168900222006696